Talanta 202 (2019) 591–599

Contents lists available at ScienceDirect

Talanta

journal homepage: www.elsevier.com/locate/talanta

MnO_2-DNAzyme-photosensitizer nanocomposite with AIE characteristic for cell imaging and photodynamic-gene therapy

Xudong Wang[a], Jun Dai[a], Xiangyu Wang[b], Qinyu Hu[b], Kaixun Huang[a], Zujin Zhao[c,**], Xiaoding Lou[b,d,***], Fan Xia[a,b,*]

[a] Hubei Key Laboratory of Bioinorganic Chemistry & Materia Medica, School of Chemistry and Chemical Engineering, Department of Obstetrics and Gynecology, Tongji Hospital Tongji Medical College, Huazhong University of Science and Technology, Wuhan, 430074, China
[b] Engineering Research Center of Nano-Geomaterials of Ministry of Education, Faculty of Materials Science and Chemistry, China University of Geosciences, Wuhan, 430074, China
[c] State Key Laboratory of Luminescent Materials and Devices, Center for Aggregation-Induced Emission, South China University of Technology, Guangzhou, 510640, China
[d] Zhejiang insitute, China University of Geosciences, Wuhan, Hangzhou, 311305, China

ARTICLE INFO

Keywords:
MnO_2
Photodynamic therapy
Gene silencing
Aggregation induced emission
DNAzyme

ABSTRACT

Photodynamic therapy (PDT) was considered as an effective treatment. Whereas only PDT is not enough to achieve effective therapy on account of irradiation intensity decreases as depth increases as well as tumor hypoxia. Combination with gene therapy and photodynamic therapy have emerged as an effective strategy to improve therapeutic effectiveness. In the present study, a GSH responsive MnO_2 was employed to delivery TB and DNAzyme for cancer imaging and PDT-gene combination treatment. TB, a photosensiters with aggregation-induced emission characteristic, was employed for photodynamic therapy, while DNAzyme, acting as catalysts for the degradation of EGR-1 mRNA, was exploited for gene silencing. All of the results of tumor treatment in vitro have implied that MnO_2-DNAzyme-TB nanocomposite (MDT) can internalize into cells. Subsequently, MDT could decrease the expression of EGR-1 by gene silencing that enabling inhibition of cell growth. In addition, the singlet oxygen which was generated by the aggregated TB were able to further suppress cell growth. Combination therapy of photodynamic as well as gene therapy greatly enhanced antitumor efficiencies. Furthermore, in vivo tumor treatment experiments demonstrated that MDT under illumination can effectively inhibit the tumor growth of MCF-7 tumor-bearing mice by photodynamic and gene silencing combination therapy.

1. Introduction

Recently, the emerging two-dimensional (2D) nanomaterial MnO_2 has been developed in a large number of fields on account of its unique features. Especially, MnO_2 nanostructures have captured much attention in bio-applications [1–8]. Organic molecules were capable of loading on the MnO_2 nanostructures through electrostatic interaction. For example, a smart delivery system for cancer diagnosis and treatment has been developed based on MnO_2 employing doxorubicin [9]. Also, MnO_2 nanostructures could strongly adsorb biomacromolecule including DNA and protein by the electrostatic interaction and π-π stacking [10–13]. Zhang and coworkers have demonstrated MnO_2 loaded Cy5-labled aptamer can be applied for cancer imaging [14]. In addition, MnO_2 nanosheets were degradable because MnO_2 can be reduced to Mn^{2+} upon the presence of GSH [15]. Furthermore, MnO_2 possess high biocompatibility as a consequence of manganese is non-toxic in biological system. Hence, MnO_2 nanosheets can be used as carrier to deliver DNA and small molecule.

Aggregation-induced emission fluorogen (AIEgen) was an emerging class of organic dyes, which show almost nonemissive in solutions whereas display bright fluorescence with high resistance to photobleaching in aggregate state [16–29]. Moreover, several AIEgens have been applied in photodynamic therapy because of its capability to generate singlet oxygen ($^1O_2$) under light irradiation [30–33]. In the

* Corresponding author. Engineering Research Center of Nano-Geomaterials of Ministry of Education, Faculty of Materials Science and Chemistry, China University of Geosciences, Wuhan, 430074, China.
** Corresponding author.
*** Corresponding author. Engineering Research Center of Nano-Geomaterials of Ministry of Education, Faculty of Materials Science and Chemistry, China University of Geosciences, Wuhan, 430074, China.
E-mail addresses: mszjzhao@scut.edu.cn (Z. Zhao), louxiaoding@cug.edu.cn (X. Lou), xiafan@hust.edu.cn, xiafan@cug.edu.cn (F. Xia).

https://doi.org/10.1016/j.talanta.2019.05.003
Received 8 February 2019; Received in revised form 10 April 2019; Accepted 2 May 2019
Available online 04 May 2019
0039-9140/

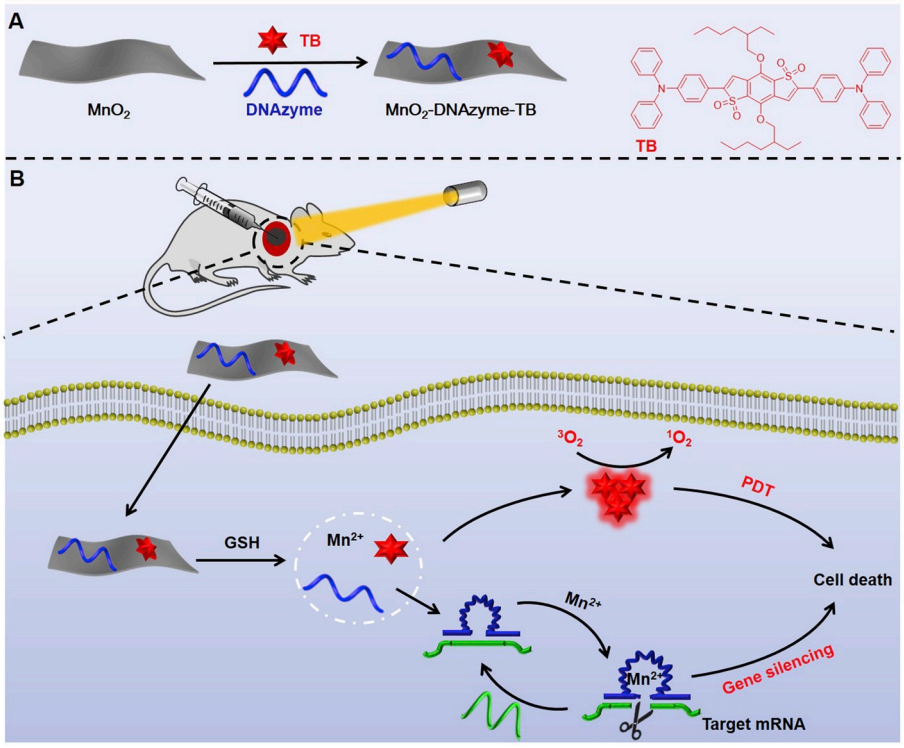

Scheme 1. Synthetic route of (A) MnO_2-DNAzyme-TB and (B) using MnO_2-DNAzyme-TB for gene silencing and photodynamic therapy.

aggregation state, traditional dyes were usually subjected to several defects such as aggregation-caused quenching as well as decreased ROS generation. Nevertheless, AIE photosensiters performed strong fluorescence and the efficacy of photosensiters increased in aggregation state because of its AIE characteristic. In spite of the unceasing breakthroughs of AIEgens in bioapplication, there is still a problem that several AIEgens were not taken up by the cells due to its poor water solubility. In order to overcome this problem, liposome [34], peptides [35–37] as well as polymer nanoparticle [38–41] have been employed as carrier for the intracellular delivery of AIEgens. In our prior study, a polymeric micelles employing AIEgens has been developed for cancer treatment via combination of both photodynamic therapy and chemotherapy [31]. Moreover, liposome and peptides have been used by our group to transport AIEgens for telomerase detection and drug release tracking [19,42–44]. Alternatively, the two-dimensional (2D) nanomaterial [45] especially the degradable MnO_2 nanosheets was an attractive alternative agent to delivery hydrophobic AIEgens into cells.

Photodynamic therapy is emerged as an effective method for cancer treatment, whereas photodynamic therapy alone is unable to completely destroy the tumor due to the weakening of the light intensity with depth and insufficient oxygen supply [46–50]. To improve the therapeutic effect, combined therapy of both photodynamic therapy and gene therapy is considered to be an effective treatment strategy. Here, photosensitizers with AIE characteristic as well as DNAzymes were loading onto GSH-responsive MnO_2 nanosheets. The nanocomposite can be used for the treatment of cancer on the basis of photodynamic and gene combination therapy. As MnO_2-DNAzyme-TB (MDT) was got into cells, MnO_2 is decomposed by GSH into Mn^{2+}, while the loaded TB and DNAzyme are released, and strongly red-fluorescence was observed due to the aggregation of hydrophobic TB in aqueous solution. Meanwhile, singlet oxygen generation ability was improved as aggregates of TB. The resulting Mn^{2+} can be used as a cofactor for DNAzymes, enabling using DNAzymes for gene knockdown. In addition, the GSH content in the cells was gradually consumed as the MnO_2 was reduced, and the ROS content increased gradually to further improve the therapeutic effect.

2. Experimental section

2.1. Materials and reagents

Tetramethylammoniam hydroxide, 2′, 7′-dichlorofluorescin diacetate (DCFH-DA) and manganese chloride tetrahydrate ($MnCl_2{\cdot}4H_2O$) were supplied by Sigma-Aldrich. The gel electrophoresis loading buffer and ladder DNA were bought from Sangon Biotech (Shanghai, China). The MCF-7 cells were supplied by China Center for Type Culture Collection. Culture medium (DMEM), fetal bovine serum and phosphate buffer saline (PBS, pH 7.4) were all provided by HyClone Thermofisher (Beijing, China). Antibody to EGR-1 and Ki 67 were obtained from Proteintech (Wuhan, China). Unless otherwise stated, other chemicals used in the experiments were obtained from Sigma-Aldrich and no further purification was required for use. The oligonucleotides used throughout all experiments were synthesized from Sangon Biotech (Shanghai, China). Water was provided by a Millipore filtration system. The sequences of the nucleic acids used in the study are shown in Table S1.

2.2. Synthesis of MnO_2 nanosheets

For further details, please see the Supporting Information.

2.3. Synthesis of DNAzyme-TB-MnO_2 nanosystem

Single-stranded DNA (ssDNA) and TB were loaded on to MnO_2 nanosheets through mixing MnO_2 nanosheets (aqueous media, 220 μL, 0.5 mg mL^{-1}) with DNAzyme (aqueous media, 5 μL, 100 μmol L^{-1}) and TB (THF, 100 μL, 150 μg mL^{-1}) in aqueous media for 40 min at room temperature. Subsequently, the above mixture was centrifuged at 10000 rpm for 20 min, and the supernatant was discarded to collect the precipitate.

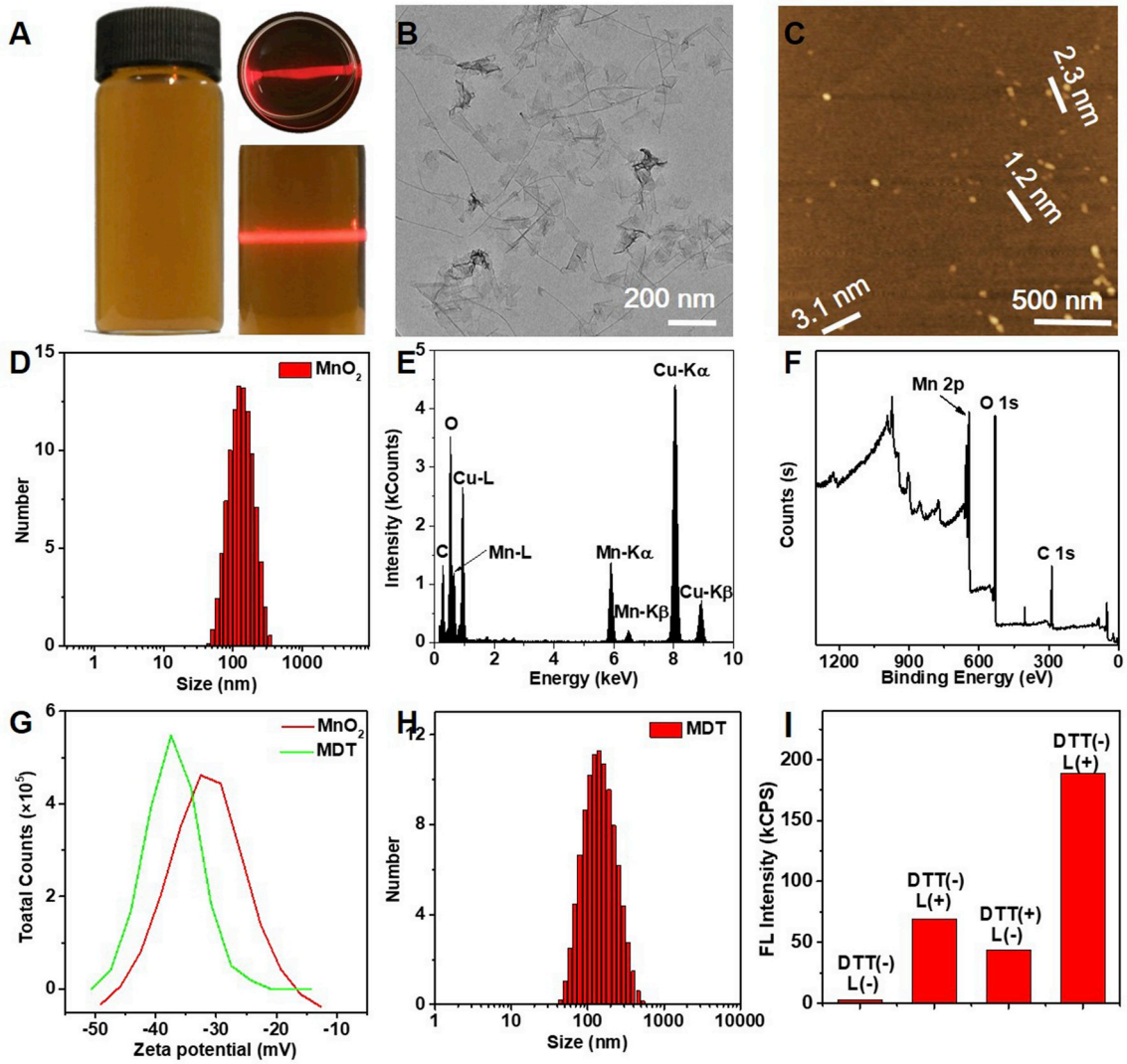

Fig. 1. (A) Digital photographs of MnO_2 nanosheets. (B) TEM image of the MnO_2 nanosheets. (C) AFM image of the MnO_2 nanosheets. (D). Dynamic light scattering analysis of MnO_2 nanosheets. (E) Energy dispersive X-ray spectroscopy analysis of the MnO_2 nanosheets. (F) XPS spectra of the MnO_2 nanosheets. (G) Zeta potential of MnO_2 nanosheets and MnO_2-DNAzyme-TB (MDT). (H). Dynamic light scattering analysis of MnO_2 nanosheets. (I) Relative fluorescence intensity of DCFH-DA in the presence of MnO_2-DNAzyme-TB treatment with or without 0.2 mM DTT.

2.4. Determination of singlet oxygen

DCFH-DA was used as fluorescent probe for the detection of ROS. The MnO_2 -DNAzyme-TB (60 μg mL^{-1}) were mixed with the 10 μmol L^{-1} DCFH-DA solution. Next, the mixture was exposed to white light (100 mW cm^{-2}) for 40 min. Thereafter, the fluorescence was recorded to monitor the generated ROS.

2.5. Cell culture

MCF-7 cells were cultured in DMEM supplemented with 10% fetal bovine serum and 1% penicillin as well as streptomycin at 37 °C in a humidified atmosphere containing 5% CO_2. Prior to the experiment, the cell density was measured through hemocytometer.

2.6. Confocal fluorescence imaging

MCF-7 cells at a density of 4×10^4 cells per well were seeded in confocal dishes, subsequently cultured at 37 °C for 24 h before experiment. After washing three times with PBS, MnO_2-DNAzyme-TB (MnO_2, MnO_2-DNAzyme or MnO_2-TB) was added into confocal dishes for 6 h.

2.7. Singlet oxygen measurement in living cells

After washing with PBS, 1 mL culture medium containing MnO_2-DNAzyme-TB (60 μg mL^{-1}) was added into cells dishes for 6 h. Subsequently, the cells was washed with 3 times. DCFH-DA was added (10 μmol L^{-1}) and the MCF-7 cells were incubated for 20 min. Next, the MCF-7 cells suspension was irradiated by light (white light, 100 mW cm^{-2}) for 20 min. The fluorescence images were performed on a confocal scanning system (Zeiss LSM 880) with an objective lens (10 ×).

2.8. Quantitative PCR

EGR-1 mRNA cDNA was employed for quantitative real-time PCR analysis. The above PCR reaction was performed on real time PCR system (Stepone Plus) by using Power SYBR Green PCR Master kit (Applied Biosystem). Supplementary Table S1 shows the sequences of PCR primers.

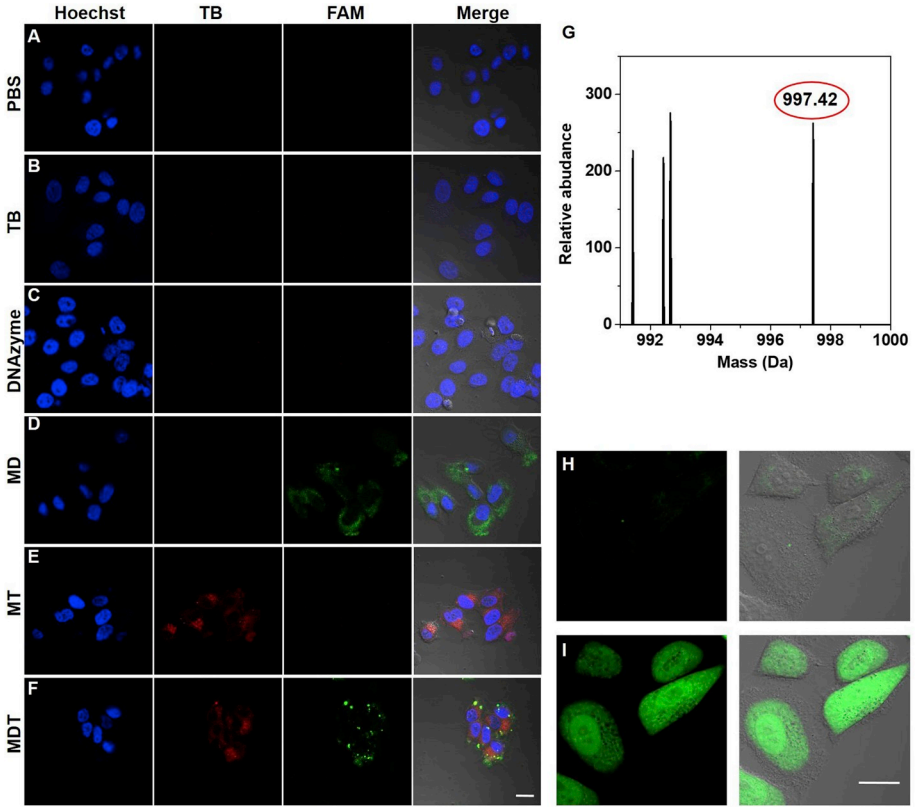

Fig. 2. Confocal fluorescence images of MCF-7 cells treated with (A) PBS, (B) TB, (C) DNAzyme, (D) MnO_2-DNAzyme (MD), (E) MnO_2-TB (MT) and (F) MnO_2-DNAzyme-TB (MDT). (G) Mass spectrum of TB from MCF-7 cells treated with MnO_2-DNAzyme-TB for 6 h. Confocal fluorescence images of ROS generation in MCF-7 cells incubated with MDT without (H) and with (H) irradiation. MCF-7 cells were incubated with MnO_2-DNAzyme-TB for 6 h followed by treatment with DCFH-DA for 15 min, respectively. Then, the cells was irradiated without (H) or with (I) white light (100 $mWcm^{-2}$) for 20 min. Scale bar: 20 μm.

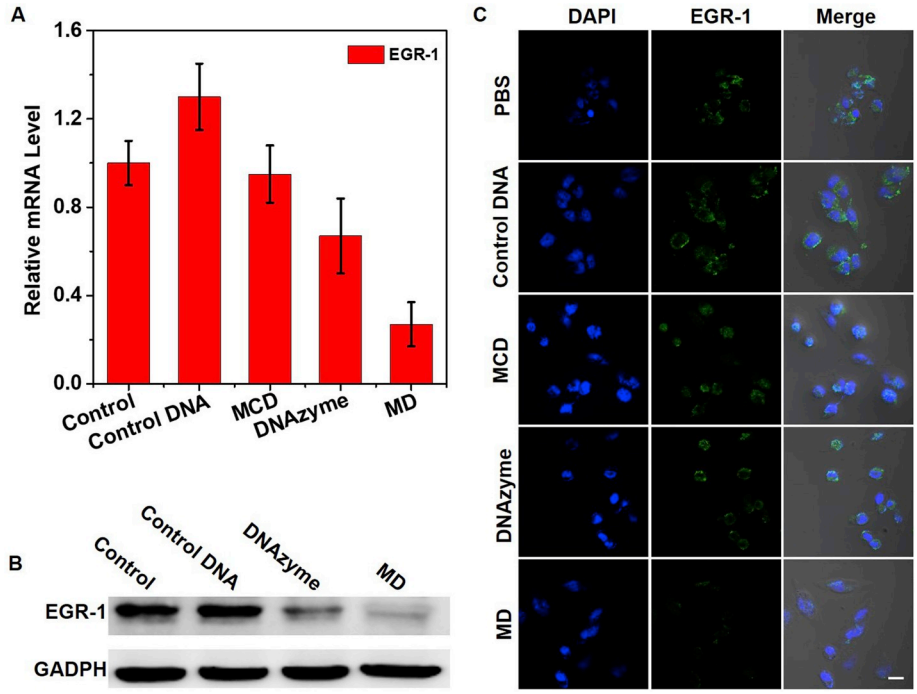

Fig. 3. (A) Real time quantitative PCR analysis of EGR-1 mRNA expression level in MCF-7 cells treated with 5 μM control DNA, MnO_2-control DNA, DNAzyme and MnO_2-DNAzyme. (B) Western blot analysis of EGR-1 protein expression in MCF-7 cells treated with control DNA, DNAzyme and MnO_2-DNAzyme. (C) Immunofluorescence analysis with antibodies against EGR-1 protein (green). After treatment, DAPI was applied for the cell nuclei were staining (blue). MCF-7 cells treated with PBS, control DNA, MnO_2-control DNA (MCD), DNAzyme and MnO_2-DNAzyme (MD). Scale bar: 20 μm. (For interpretation of the references to colour in this figure legend, the reader is referred to the Web version of this article.)

2.9. Immunofluorescence assays

MCF-7 cells at a density of 4×10^4 cells per well were seeded in confocal dishes before experiment. Subsequently, MCF-7 cells were incubated with control DNA, MnO_2-control DNA, DNAzyme as well as MnO_2-DNAzyme. After 6 h incubation, washing buffer was employed to wash cells 3 times. After 48 h of treatment, the cells were then fixed in 4% paraformaldehyde for 15 min, followed by permeabilized with 0.2% Triton X-100 in PBS for 15 min. Thereafter, cells were blocked for nonspecific binding with 5% BSA and treated with *anti*-EGR-1 (1:100) antibody overnight. Washing buffer was employed to wash MCF-7 cells 3 times with, and the cells were treated by using secondary antibody (goat anti-rabbit IgG) which were labeled with Alexa Fluor 488 (1:1000) for 1 h at room temperature. The cells are thereafter incubated with DAPI prior to imaging. Immunofluorescence images were performed on a Zeiss LSM 880 confocal scanning system. For each channel,

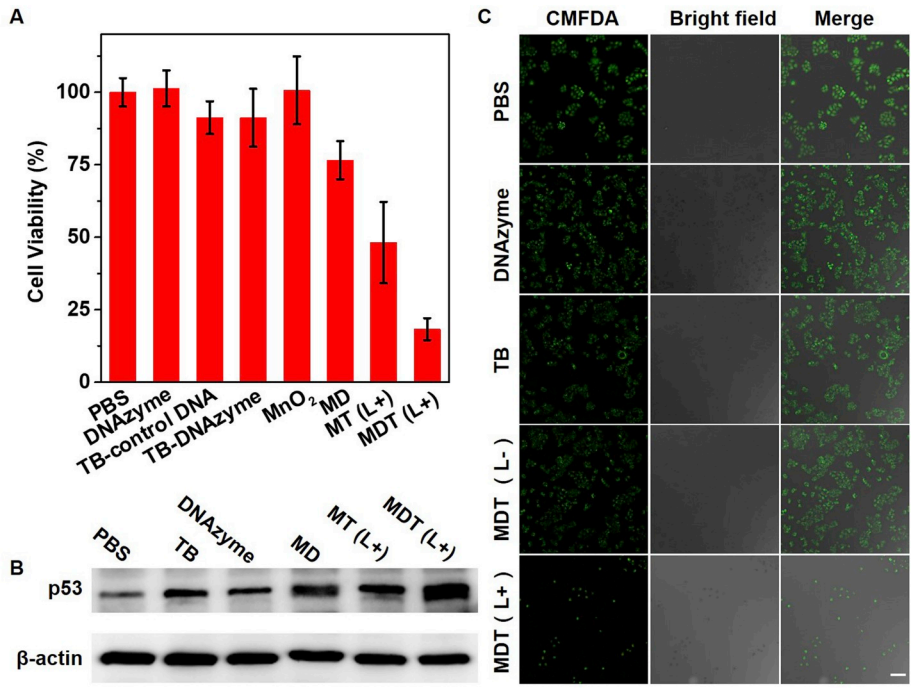

Fig. 4. (A) Cell viability of MCF-7 cells after treatment with PBS, DNAzyme, TB-control DNA, TB-DNAzyme, MnO_2, MnO_2-DNAzyme (MD), MnO_2-TB with irradiation (MT) and MnO_2-DNAzyme-TB with irradiation (MDT). (B) Western blot analysis of p53-related protein expression in MCF-7 cells after treatment with PBS, TB, DNAzyme, MnO_2-DNAzyme (MD), MnO_2-TB with irradiation (MT) and MnO_2-DNAzyme-TB with irradiation (MDT). (C) Cell apoptosis imaging after treatment with PBS, DNAzyme, TB, MnO_2-DNAzyme-TB without irradiation (MDT (L-)) and with irradiation (MDT (L+)) for 20 min (White light, 100 mW/cm^{-2}). Scale bar: 100 μm.

all images use the same settings.

2.10. Cytotoxicity assays

The cytotoxicity of MnO_2 and MnO_2-DNAzyme-TB on MCF-7 cells were measured by standard MTT assays. MCF-7 cells at the density of 5×10^3 cells per wells were seeded in 96-well plates. After incubation for 24 h, the cells were then incubated with different concentrations of MnO_2 (0–80 μg mL^{-1}) for 24 h. Next, 20 μL MTT solution (5 mg mL^{-1}) was added into each well incubated at 37 °C for 4 h. The medium containing samples were removed after 4 h, subsequently 150 μL of dimethyl sulphoxide was added to each well. The optical density of the wells at 570 nm was obtained by using a microplate reader.

2.11. Animal experiments

Nude mice (20 g) were supplied by HFK Bioscience Co., and handling procedures involving animals were according to the guidelines of the Animal Care Committee at Tongji Medical College. MCF-7 cells tumor-bearing mice were established as the animal model for in vivo therapeutic studies. Afterwards, 1 million MCF-7 cells (1×10^6 cells, 100 μL) were subcutaneously injected into the oxter region of mice.

2.12. In vivo photodynamic therapy

When the tumor volumes reached approximately 70 mm^3, the treatment was performed. All mice were randomly divided into five groups (n = 3 mice/group): (1) PBS; (2) MnO_2; (3) MnO_2-DNAzyme; (4) MnO_2-TB + light; and (5) MnO_2-DNAzyme-TB + light. The mice was intratumorally injected with the above solution (100 μL, 2 mg mL^{-1}). After 24 h, laser treatment (with a 532 nm laser (250 mW cm^{-2})) were conducted for 20 min. In the meanwhile, the tumor size as well as body weight were conducted daily. The mice were killed after 2 weeks treatment, subsequently the tumors were collected, followed by taking photograph.

2.13. Histology

For histology, MCF-7 tumor tissues were isolated from mice 24 h after the last treatment. The mice were killed after the 2 weeks' treatment. The major organs as well as tumors of various groups were dissected and fixed in 4% paraformaldehyde for further H&E staining.

2.14. Immunohistochemistry staining

The expression of EGR-1 and Ki 67 in tumor tissues was determined by immunohistochemistry. Sections were stained with rabbit *anti*-EGR-1 and *anti*-Ki 67 antibodies at 4 °C overnight. Subsequently, the immunoreactivity was visualized via the reaction between streptavidin-biotin-peroxidase complex and diaminobenzidine.

3. Results and discussion

The MnO_2 nanosheets was prepared according to the previous report. Typically, the bulk MnO_2 was initially synthesized by utilizing the redox reaction between H_2O_2 and $MnCl_2$ in the presence of tetramethylammonium hydroxide. Subsequently, the MnO_2 nanosheets was synthesized via liquid exfoliation strategy from bulk MnO_2 (Scheme 1A). As shown in Fig. 1A, the typical Tyndall effect in the representative picture of MnO_2 exhibited high dispersity in aqueous media which demonstrated its good hydrophilicity. The morphology of the synthesized MnO_2 nanosheets was accessed by the transmission electron microscopy (TEM). As shown in Fig. 1B, the TEM image indicated highly dispersed ultrathin and electron-transparent 2D flakes of MnO_2 nanosheets. The average thickness of MnO_2 nanosheets was evaluated by atomic force microscopy (AFM). As can be seen in Fig. 1C, AFM height image provided further evidence that the thickness of MnO_2 nanosheets was 2.2 ± 0.9 nm. The size of MnO_2 measured by dynamic light scattering (DLS) was about 103.8 ± 1.4 nm (Fig. 1D and Fig. S1). The chemical composition of MnO_2 was confirmed by EDS and X-ray photoelectron spectroscopy (XPS). The chemical composition of MnO_2 was verified by energy-dispersive spectroscopy (Fig. 1E) as well as the X-ray photoelectron spectroscopy (XPS) which demonstrated the presence of Mn and O element. In addition, the MnO_2 displayed the two strong binding energy peaks at 653.8 and 642.2 eV (Fig. S2), which could be ascribed to Mn 2p1/2 and Mn 2p3/2, respectively. Taking together, the aforementioned results demonstrated the successful fabrication of MnO_2.

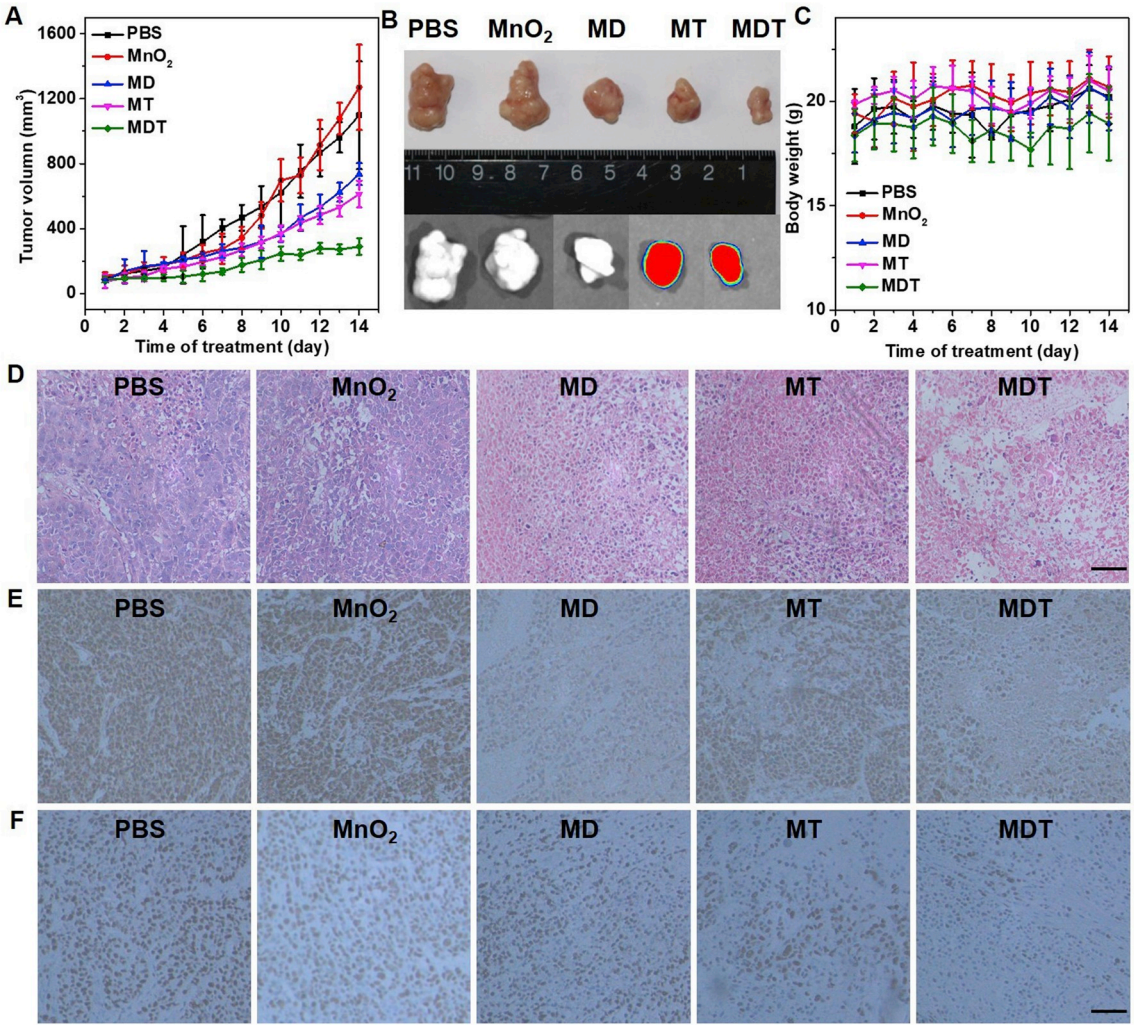

Fig. 5. (A) Changes in tumor volumes after different treatment by intratumoural injection. (B) Digital photograph (upper) and ex vivo fluorescence imaging (down) of tumor dissection. (C) Body weight of mice in different groups. (D) H&E staining of the tumor sections harvested from various groups after treatment. (E) Immunohistochemistry for Ki-67 of tumor from various groups. (F) Immunohistochemistry for EGR-1 of tumor from various groups. Scale bar: 50 μm.

The ultrathin thickness endow MnO_2 with high specific surface area, which has been confirmed by BET. As can be seen from Fig. S3, the BET surface area of MnO_2 was 51.1 $cm^3\,g^{-1}$, which was comparable with the literature [51]. By taking advantage of the above unique feature, those nanomaterial have been applied widely as vector for cancer treatment, the potential cargo-loading capacity of MnO_2 were then explored. Different concentrations of manganese dioxide were mixed with 2 μg mL^{-1} TB. Because MnO_2 nanosheets exhibited the excellent absorbability and quenching effect in visible light region, manganese dioxide was capable of quenching TB. When the concentration of manganese dioxide reaches 72 μg mL^{-1}, the fluorescence of TB can be completely quenched (Fig. S4A). At this concentration, the equivalent of 1 μg of MnO_2 nanosheets can adsorption 27.7 pg of TB. Similarly, once the concentration of manganese dioxide reaches 20 μg mL^{-1}, 100 nM FAM-labled DNAzyme can completely quenching (Fig. S4B). When the concentration of manganese dioxide achieve this, the equivalent of 1 mg manganese dioxide adsorption 5 pmol of DNAzyme. DNAzyme and TB have successfully loaded onto the surface of MnO_2 through electrostatic interaction and π-π stacking. Zeta potential was used to verify the formation of MDT via the changes in the surface charge. Compared to the surface charge of the MnO_2, the zeta potential of MDT varied from −30.9 to −39 mV as shown in Fig. 1G, which was attributed to the existence of negative charged DNAzyme in the MDT. As shown in Fig. 1H and Fig. S5, the average hydrodynamic diameter of MDT was measured by DLS to be 109.9 ± 3.6 nm. The size of MDT has hardly changed in comparison with MnO_2. Therefore, the above results indicated the successful preparation of MDT.

The fluorescence of TB (Fig. S6A) and FAM-modified DNAzymes (Fig. S6B) gradually increases as the concentration of DTT increases, indicating that TB and DNAzyme were released as MnO_2 was degraded into Mn^{2+} in the present of reducing substance. Owing to its hydrophobicity, the released TB formed aggregates, and thereby the bright fluorescence could be observed as well as the generating singlet oxygen ability was improved. DCFH-DA was used as a singlet oxygen probe to detect singlet oxygen. As shown in Figs. S7A and a slight fluorescence was observed in MnO_2-DNAzyme-TB solution in the presence of DCFH-DA. Upon light irradiation, the fluorescence intensity continuously enhanced overtime. With the addition of 0.2 mM DTT, a rapid increase of fluorescence signal was observed as the light irradiation time went on (Fig. 1I and Fig. S7B). The fluorescence of DCFH-DA in the presence of MnO_2-TB-DNAzyme was enhanced 69-fold after 40 min compared with no light illumination and no DTT sample. The above results showed that MnO_2 could effectively suppress the fluorescence and singlet oxygen generation efficiency of TB. Furthermore, the average diameter of MDT was 194 ± 8.6 nm in the presence of DTT, which further verified the presence of TB aggregates, as can be seen in Fig. S8. As shown in Fig. S9, only one band was observed from gel electrophoresis, demonstrating that mRNA was efficiently degraded by

DNAzyme in the presence of Mn^{2+}. However, the mRNA cannot be degraded by DNAzyme in the absence of Mn^{2+}. The above results indicated that TB and DNAzyme loaded on MDT was released by introduction of a reducing substance, enabling singlet oxygen generating ability as well as target mRNA degradation ability were improved.

Next, the intracellular delivery of MDT into MCF-7 cells as well as intracellular singlet oxygen generation was further indicated by CLSM. First, cytotoxicity of MnO_2 was tested on MCF-7 cells through MTT assay. As shown in Fig. S10, it can be observed that there was no obvious toxicity when the concentration of manganese dioxide reached 60 μg mL^{-1}, proving low cytotoxicity of MnO_2. As shown in Fig. 2B and C, negligible fluorescence were visualized when MCF-7 cells were treated with TB or DNAzyme for 6 h. That can be ascribed to the hydrophobicity of TB, therefore TB has trouble entering the MCF-7 cells. In contrast, a significant fluorescence signal was observed after treatment with MD (Fig. 2D), MT (Fig. 2E) and MDT (Fig. 2F), suggesting that MDT were successfully taken up by MCF-7 cells. In addition, the mass spectra demonstrated the released product from MDT treated MCF-7 cells, which further indicated the presence of TB in cells (Fig. 2G). MnO_2 was degraded by intracellular GSH, enabling the release of TB and DNAzyme. Afterwards, the generation of singlet oxygen in MCF-7 cells was further determined by using a classical $^1O_2$ fluorescence probe (DCFH-DA). As shown in Fig. 2H and Fig. S11B, weak emissive was observed in the absence of light. Conversely, DCFH-DA showed the bright green fluorescence signal in the MDT treated MCF-7 cells under light irradiation for 20 min, indicating a large amount of singlet oxygen production in the cells (Fig. 2I and Fig. S11C). As a consequence, these results indicated that MnO_2 can serve as degradable vector to load TB and DNAzyme.

Although PDT was considered as a promising therapeutic strategy for a variety of cancers [15]. However, the effectiveness of PDT was impaired owing to tumor hypoxia. Thus, gene silencing was an alternative approach to ameliorate the treatment effect. EGR-1m RNA was selected as target for DNAzyme degradation. Therefore, PCR, Western blot and immunofluorescence were carried out to assess the feasibility of MDT for down-regulation of EGR-1 in MCF-7 cells. Quantitative real-time PCR was used to determine the expression of EGR-1 mRNA in MCF-7 cells incubated with or without MnO_2-DNAzyme. As shown in Fig. 3A, EGR-1 was significantly reduced expressed in MCF-7 cells after treatment with MnO_2-DNAzyme. However, there was no significant change of the EGR-1 mRNA expression in MCF-7 cells treated with equivalent quantities of control DNA and control DNA-MnO_2. Western-blot was further used to investigate the expression of EGR-1 protein in MCF-7 cells cultured with MnO_2-DNAzyme. As shown in Fig. 3B, the EGR-1 protein expression was drastically reduced in the MnO_2-DNAzyme group, which is in agreement with RT-PCR. The expression of EGR-1 protein was further analyzed by immunofluorescence. As shown in Fig. 3C, negligible fluorescent signal was observed in the MnO_2-DNAzymes treated MCF-7 cells by using the fluorescent dyes labeled EGR-1 antibody in comparison with other groups, which was attributed to effective gene knockdown of EGR-1 mRNA. In addition, as the concentration of MnO_2-DNAzyme increased, the survival rate of the cells gradually decreased (Fig. S12). Whereas there was no significant change in the survival rate of DNAzyme alone. This further demonstrated that MnO_2-DNAzyme can degrade EGR-1 mRNA and down-regulate the expression of EGR-1. Collectively, the above results demonstrated that MDT can serve as vector for delivery DNAzyme as well as gene silencing.

The gene silencing and photodynamic therapy of MDT in MCF-7 cells were examined. As shown in Fig. 4A, the MCF-7 cells was incubated with MDT for 6 h, followed by white light irradiation. Apparently, the cell viability of MCF-7 cells was the lowest after treatment with MDT subjected to illumination. There was much higher cytotoxicity observed in MCF-7 cells treated with MD and MT than that of control group. In contrast, almost no cytotoxicity toward MCF-7 cells was observed among the four groups (single DNAzyme, TB-control DNA without light irradiation, TB-DNAzyme without light irradiation and MnO_2). Thus, the combination therapy further improved the treatment outcome compared with the PDT only. To further assess the cytotoxicity of MDT, western blot was used to analyze the expression of p53-related protein after gene silencing and photodynamic therapy. β-Actin acts as an internal reference and its expression remains unchanged. As shown in Fig. 4B, MCF-7 cells incubated with MDT displayed the highest p53-related protein expression in comparison with the other groups, which was owing to the combination therapy of both gene silencing and photodynamic therapy. And the expression of p53 in those of treated with MD and MT were higher than in the control groups. It was because of gene silencing in MD group and photodynamic therapy in MT group, thus resulting in higher p53 protein expression. It can also be seen from the confocal laser images (Fig. 4C) that the number of living cells in the MDT (L+)-treated MCF-7 cells was dramatically reduced. The reverse results were obtained in other groups, demonstrating either low delivery efficiency of DNAzyme, TB or no obvious cytotoxicity of MDT without irradiation in MCF-7 cells. From the results, we can demonstrated that MDT could be used as a therapeutic agent to achieve gene therapy and photodynamic combination therapy.

In view of the encouraging results in vitro system, therapeutic outcome of combination both TB-based PDT and DNAzyme-based gene silencing in vivo were thereafter evaluated by using the MCF-7 mouse xenograft. The subcutaneous tumor models was established through implanting MCF-7 cells at the armpits of nude mice, respectively. When the average tumor volume of mice reached about 70 mm^3, mice were divided into 5 groups: PBS, MnO_2, MnO_2-DNAzyme (MD), MnO_2-TB (MT) and MnO_2-DNAzyme-TB (MDT (L+)). The fluorescence signal of the tumor in the MT and MDT groups increased significantly as time extended after intratumoral injection, which mainly resulted from that the MnO_2 was gradually reduced by intracellular GSH to Mn^{2+} and then releasing TB (Figs. S13A and B). The PBS, MnO_2 and MD groups did not have fluorescent signal due to the absence of TB. The absence of fluorescent signals in other organs of the mouse indicates that the nanocomposite have a good enrichment effect at tumor site. Photodynamic therapy was performed 24 h after the intratumoral injection, and the mice were exposed to a 532 nm light with an irradiance of 250 mW cm^{-2} for 20 min. After treatments, the tumor volume and weight were measured every day to monitor its therapeutic effect. It is evident from Fig. 5A that tumor volume of the PBS treated mice increased 13.8-fold during the treatment period. At day 14 of treatment, MT injection with irradiation or MD injection could reduce tumor growth. Importantly, MDT injection followed by irradiation were able to greatly suppress tumor growth, respectively. This demonstrated an obvious therapeutic effect of MDT (L+) in vivo. In addition, mice in the group treated MnO_2 did not show obvious tumor inhibition versus the PBS group. Similar results were obtained from the representative photographs of corresponding tumor tissues in various group (Fig. 5B). The bright fluorescence was observed in tumors of MT and MDT (L+) group (Fig. 5B and Fig. S14) owing to the TB being released from the nanocomposite. No significant change in the weight of the mice were observed during two weeks (Fig. 5C). As demonstrated in Fig. 5D, hematoxylin and eosin (H&E) stained tumor sections further confirmed that most of the cancer cells in the MD, MT (L+) and MDT (L+) groups were severely damaged, while the cells of the corresponding control group remained partially or mostly normal morphology. Taken together, all the results herein demonstrated that the good therapeutic effect was achieved after combined treatment with MDT. As shown in Fig. S15, no obvious abnormality was observed in H&E stained major organ tissues of mice indicated that the above materials had almost no side effects on mice. The expression of EGR-1 in various groups was further analyzed by EGR-1 immunohistochemistry. As can be seen from Fig. 5E, the expression of EGR-1 protein significantly decreased in the MD and MDT (L+) groups compared with the control group. The expression of EGR-1 protein in MnO_2 and MT (L+) group is similar to that of PBS group. It was further proved that DNAzme in the MD and MDT (L

+) groups can effectively degrade EGR-1 mRNA. As shown in Fig. 5F and Fig. S16, the Ki 67 content in the MD, MT (L+) and MDT (L+) groups was down-regulated than that of PBS group. While significant decrease of Ki 67 was observed in MDT (L+) group coupling with illumination because of the antitumor effect of MDT nanocomposite. Thus, the above results indicated that MDT (L+) nanocomposite has shown a potential antitumor efficacy upon light irradiation.

4. Conclusions

In conclusion, we have successfully developed MnO_2-DNAzyme-TB nanocomposite as a GSH responsive therapeutic agent for cancer imaging and treatment. Photosensitizers (TB) with aggregation-induced emission (AIE) characteristic decorated onto MnO_2 nanosheets through electrostatic interaction and π-π stacking. Nevertheless, PDT alone was not enough for tumor treatment on account of the unavoidable depth-pendent reduction of light intensity as well as tumor hypoxia. To address the aforementioned shortcoming, gene silencing was an alternative approach to improve the treatment effect. Mn^{2+}-dependent DNAzyme loading MnO_2 nanosheets could be used to negatively regulate the gene expression. Moreover, the use of combinatorial not only PDT agent but also gene agent have been demonstrated an effective approach to increase therapeutic efficacy. Once the MDT was internalized into the cancers cells, MnO_2 degrades to Mn^{2+} owing to intracellular GSH consequent TB and DNAzyme release. And then the fluorescence of TB recovered and produced singlet oxygen under irradiation, leading to apoptosis. In addition, the produced Mn^{2+} ions serves as cofactors of DNAzyme for cleaving EGR-1 mRNA, enabling inhibition of cell growth. When MnO_2 was present, the GSH contents decreased and the ROS contents increased accordingly, leading to improve outcome of PDT therapy. The MnO_2-DNAzyme-TB nanocomposite holds great promise as combinatorial cancer therapeutic agent for tumor treatment.

Acknowledgements

This work was supported by the National Natural Science Foundation of China (21788102, 21525523, 21722507, 21574048 and 21874121), the National Basic Research Program of China (973 Program, 2015CB932600), the National Key R&D Program of China (2016YFF0100800 and 2017YFA0208000), Natural Science Foundation of Zhejiang Province of China (LY18B050002). .

Appendix A. Supplementary data

Supplementary data to this article can be found online at https://doi.org/10.1016/j.talanta.2019.05.003.

References

[1] J. Ge, R. Cai, X. Chen, Q. Wu, L. Zhang, Y. Jiang, C. Cui, S. Wan, W. Tan, Facile approach to prepare HSA-templated MnO_2 nanosheets as oxidase mimic for colorimetric detection of glutathione, Talanta 195 (2019) 40–45.
[2] R. Deng, X. Xie, M. Vendrell, Y.-T. Chang, X. Liu, Intracellular glutathione detection using MnO_2-nanosheet-modified upconversion nanoparticles, J. Am. Chem. Soc. 133 (2011) 20168–20171.
[3] X.-a. Yang, M.-t. Shi, D. Leng, W.-b. Zhang, Fabrication of a porous hydrangea-like Fe_3O_4@MnO_2 composite for ultra-trace arsenic preconcentration and determination, Talanta 189 (2018) 55–64.
[4] Y. Haldorai, K. Giribabu, S.-K. Hwang, C.H. Kwak, Y.S. Huh, Y.-K. Han, Facile synthesis of α-MnO_2 nanorod/graphene nanocomposite paper electrodes using a 3D precursor for supercapacitors and sensing platform to detect 4-nitrophenol, Electrochim. Acta 222 (2016) 717–727.
[5] Y. Han, Y. Yu, L. Zhang, L. Huang, J. Zhai, S. Dong, Facile synthesis of Ni based metal-organic frameworks wrapped MnO_2 nanowires with high performance toward electrochemical oxygen evolution reaction, Talanta 186 (2018) 154–161.
[6] F. Qu, H. Pei, R. Kong, S. Zhu, L. Xia, Novel turn-on fluorescent detection of alkaline phosphatase based on green synthesized carbon dots and MnO_2 nanosheets, Talanta 165 (2017) 136–142.
[7] W. Fan, W. Bu, B. Shen, Q. He, Z. Cui, Y. Liu, X. Zheng, K. Zhao, J. Shi, Intelligent MnO_2 nanosheets anchored with upconversion nanoprobes for concurrent pH-/H_2O_2-responsive UCL imaging and oxygen-elevated synergetic therapy, Adv. Mater. 27 (2015) 4155–4161.
[8] J. Li, D. Li, R. Yuan, Y. Xiang, Biodegradable MnO_2 nanosheet-mediated signal amplification in living cells enables sensitive detection of down-regulated intracellular microRNA, ACS Appl. Mater. Interfaces 9 (2017) 5717–5724.
[9] Y. Chen, D. Ye, M. Wu, H. Chen, L. Zhang, J. Shi, L. Wang, Break-up of two-dimensional MnO_2 nanosheets promotes ultrasensitive pH-triggered theranostics of cancer, Adv. Mater. 26 (2014) 7019–7026.
[10] F. Chen, M. Bai, K. Cao, Y. Zhao, J. Wei, Y. Zhao, Fabricating MnO_2 nanozymes as intracellular catalytic DNA circuit generators for versatile imaging of base-excision repair in living cells, Adv. Funct. Mater. 27 (2017) 1702748.
[11] H. Fan, Z. Zhao, G. Yan, X. Zhang, C. Yang, H. Meng, Z. Chen, H. Liu, W. Tan, A smart DNAzyme- MnO_2 nanosystem for efficient gene silencing, Angew. Chem. Int. Ed. 54 (2015) 4801–4805.
[12] C.R. Gordijo, A.Z. Abbasi, M.A. Amini, H.Y. Lip, A. Maeda, P. Cai, P.J. O'Brien, R.S. DaCosta, A.M. Rauth, X.Y. Wu, Design of hybrid MnO_2-polymer-lipid nanoparticles with tunable oxygen generation rates and tumor accumulation for cancer treatment, Adv. Funct. Mater. 25 (2015) 1858–1872.
[13] L. Han, P. Liu, H. Zhang, F. Li, A. Liu, Phage capsid protein-directed MnO_2 nanosheets with peroxidase-like activity for spectrometric biosensing and evaluation of antioxidant behaviour, Chem. Commun. 53 (2017) 5216–5219.
[14] Z. Zhao, H. Fan, G. Zhou, H. Bai, H. Liang, R. Wang, X. Zhang, W. Tan, Activatable fluorescence/MRI bimodal platform for tumor cell imaging via MnO_2 nanosheet–aptamer nanoprobe, J. Am. Chem. Soc. 136 (2014) 11220–11223.
[15] H. Fan, G. Yan, Z. Zhao, X. Hu, W. Zhang, H. Liu, X. Fu, T. Fu, X.B. Zhang, W. Tan, A smart photosensitizer-manganese dioxide nanosystem for enhanced photodynamic therapy by reducing glutathione levels in cancer cells, Angew. Chem. Int. Ed. 55 (2016) 5477–5482.
[16] H.-T. Feng, Y.-X. Yuan, J.-B. Xiong, Y.-S. Zheng, B.Z. Tang, Macrocycles and cages based on tetraphenylethylene with aggregation-induced emission effect, Chem. Soc. Rev. 47 (2018) 7452–7476.
[17] X. Gu, R.T. Kwok, J.W. Lam, B.Z. Tang, AIEgens for biological process monitoring and disease theranostics, Biomaterials 146 (2017) 115–135.
[18] J. Qian, B.Z. Tang, AIE luminogens for bioimaging and theranostics: from organelles to animals, Chem 3 (2017) 56–91.
[19] Y. Zhuang, M. Zhang, B. Chen, R. Duan, X. Min, Z. Zhang, F. Zheng, H. Liang, Z. Zhao, X. Lou, Quencher group induced high specificity detection of telomerase in clear and bloody urines by AIEgens, Anal. Chem. 87 (2015) 9487–9493.
[20] X. Wang, J. Dai, X. Min, Z. Yu, Y. Cheng, K. Huang, J. Yang, X. Yi, X. Lou, F. Xia, DNA-conjugated amphiphilic aggregation-induced emission probe for cancer tissue imaging and prognosis analysis, Anal. Chem. 90 (2018) 8162–8169.
[21] Y. Cheng, C. Sun, X. Ou, B. Liu, X. Lou, F. Xia, Dual-targeted peptide-conjugated multifunctional fluorescent probe with AIEgen for efficient nucleus-specific imaging and long-term tracing of cancer cells, Chem. Sci. 8 (2017) 4571–4578.
[22] X. Min, Y. Zhuang, Z. Zhang, Y. Jia, A. Hakeem, F. Zheng, Y. Cheng, B.Z. Tang, X. Lou, F. Xia, Lab in a tube: sensitive detection of MicroRNAs in urine samples from bladder cancer patients using a single-label DNA probe with AIEgens, ACS Appl. Mater. Interfaces 7 (2015) 16813–16818.
[23] Y. Cheng, J. Dai, C. Sun, R. Liu, T. Zhai, X. Lou, F. Xia, An intracellular H_2O_2-responsive AIEgen for the peroxidase-mediated selective imaging and inhibition of inflammatory cells, Angew. Chem. Int. Ed. 57 (2018) 3123–3127.
[24] Z. Zhu, J. Qian, X. Zhao, W. Qin, R. Hu, H. Zhang, D. Li, Z. Xu, B.Z. Tang, S. He, Stable and size-tunable aggregation-induced emission nanoparticles encapsulated with nanographene oxide and applications in three-photon fluorescence bioimaging, ACS Nano 10 (2015) 588–597.
[25] J. Guo, X.L. Li, H. Nie, W. Luo, S. Gan, S. Hu, R. Hu, A. Qin, Z. Zhao, S.J. Su, Achieving high-performance nondoped OLEDs with extremely small efficiency roll-off by combining aggregation-induced emission and thermally activated delayed fluorescence, Adv. Funct. Mater. 27 (2017) 1606458.
[26] A. Nicol, R.T. Kwok, C. Chen, W. Zhao, M. Chen, J. Qu, B.Z. Tang, Ultrafast delivery of aggregation-induced emission nanoparticles and pure organic phosphorescent nanocrystals by saponin encapsulation, J. Am. Chem. Soc. 139 (2017) 14792–14799.
[27] Z. Song, D. Mao, S.H. Sung, R.T. Kwok, J.W. Lam, D. Kong, D. Ding, B.Z. Tang, Activatable fluorescent nanoprobe with aggregation-induced emission characteristics for selective in vivo imaging of elevated peroxynitrite generation, Adv. Mater. 28 (2016) 7249–7256.
[28] Y. Cheng, C. Sun, R. Liu, J. Yang, J. Dai, T. Zhai, X. Lou, F. Xia, A multifunctional peptide-conjugated AIEgen for efficient and sequential targeted gene delivery into the nucleus, Angew. Chem.Int. Ed. 58 (2019) 5049–5053.
[29] F. Wu, X. Wu, Z. Duan, Y. Huang, X. Lou, F. Xia, Biomacromolecule-functionalized AIEgens for advanced biomedical studies, Small (2019) 1804839.
[30] M. Jiang, R.T. Kwok, X. Li, C. Gui, J.W. Lam, J. Qu, B.Z. Tang, A simple mitochondrial targeting AIEgen for image-guided two-photon excited photodynamic therapy, J. Mater. Chem. B 6 (2018) 2557–2565.
[31] X. Yi, J. Dai, Y. Han, M. Xu, X. Zhang, S. Zhen, Z. Zhao, X. Lou, F. Xia, A high therapeutic efficacy of polymeric prodrug nano-assembly for a combination of photodynamic therapy and chemotherapy, Commun. Biol. 1 (2018) 202.
[32] S. Zhen, S. Wang, S. Li, W. Luo, M. Gao, L.G. Ng, C.C. Goh, A. Qin, Z. Zhao, B. Liu, Efficient red/near-infrared fluorophores based on Benzo [1, 2-b: 4, 5-b′] dithiophene 1, 1, 5, 5-tetraoxide for targeted photodynamic therapy and in vivo two-photon fluorescence bioimaging, Adv. Funct. Mater. 28 (2018) 1706945.
[33] X. Gu, X. Zhang, H. Ma, S. Jia, P. Zhang, Y. Zhao, Q. Liu, J. Wang, X. Zheng, J.W. Lam, Corannulene-incorporated AIE nanodots with highly suppressed non-radiative decay for boosted cancer phototheranostics in vivo, Adv. Mater. (2018)

1801065.
[34] X. Zhang, B. Wang, Y. Xia, S. Zhao, Z. Tian, P. Ning, Z. Wang, In vivo and in situ activated aggregation-induced emission probes for sensitive tumor imaging using tetraphenylethene-functionalized trimethincyanines-encapsulated liposomes, ACS Appl. Mater. Interfaces 10 (2018) 25146–25153.
[35] Q. Hu, M. Gao, G. Feng, B. Liu, Mitochondria-targeted cancer therapy using a light-up probe with aggregation-induced-emission characteristics, Angew. Chem. Int. Ed. 53 (2014) 14225–14229.
[36] X. Liu, G. Liang, Dual aggregation-induced emission for enhanced fluorescence sensing of furin activity in vitro and in living cells, Chem. Commun. 53 (2017) 1037–1040.
[37] S. Ji, H. Gao, W. Mu, X. Ni, X. Yi, J. Shen, Q. Liu, P. Bao, D. Ding, Enzyme-instructed self-assembly leads to the activation of optical properties for selective fluorescence detection and photodynamic ablation of cancer cells, J. Mater. Chem. B 6 (2018) 2566–2573.
[38] Y. Gao, G. Feng, T. Jiang, C. Goh, L. Ng, B. Liu, B. Li, L. Yang, J. Hua, H. Tian, Biocompatible nanoparticles based on diketo-pyrrolo-pyrrole (DPP) with aggregation-induced red/NIR emission for in vivo two-photon fluorescence imaging, Adv. Funct. Mater. 25 (2015) 2857–2866.
[39] S. Xu, Y. Yuan, X. Cai, C.-J. Zhang, F. Hu, J. Liang, G. Zhang, D. Zhang, B. Liu, Tuning the singlet-triplet energy gap: a unique approach to efficient photosensitizers with aggregation-induced emission (AIE) characteristics, Chem. Sci. 6 (2015) 5824–5830.
[40] S.S. Liow, Q. Dou, D. Kai, Z. Li, S. Sugiarto, C.Y.Y. Yu, R.T.K. Kwok, X. Chen, Y.L. Wu, S.T. Ong, Long-term real-time in vivo drug release monitoring with AIE thermogelling polymer, Small 13 (2017) 1603404.
[41] W. Wu, G. Feng, S. Xu, B. Liu, A photostable far-red/near-infrared conjugated polymer photosensitizer with aggregation-induced emission for image-guided cancer cell ablation, Macromolecules 49 (2016) 5017–5025.
[42] Y. Zhuang, C. Shang, X. Lou, F. Xia, Construction of AIEgens-based bioprobe with two fluorescent signals for enhanced monitor of extracellular and intracellular telomerase activity, Anal. Chem. 89 (2017) 2073–2079.
[43] Y. Cheng, F. Huang, X. Min, P. Gao, T. Zhang, X. Li, B. Liu, Y. Hong, X. Lou, F. Xia, Protease-responsive prodrug with aggregation-induced emission probe for controlled drug delivery and drug release tracking in living cells, Anal. Chem. 88 (2016) 8913–8919.
[44] Y. Zhuang, Q. Xu, F. Huang, P. Gao, Z. Zhao, X. Lou, F. Xia, Ratiometric fluorescent bioprobe for highly reproducible detection of telomerase in bloody urines of bladder cancer patients, ACS Sens. 1 (2016) 572–578.
[45] C. Zhu, Z. Zeng, H. Li, F. Li, C. Fan, H. Zhang, Single-layer MoS2-based nanoprobes for homogeneous detection of biomolecules, J. Am. Chem. Soc. 135 (2013) 5998–6001.
[46] Y. Xu, Z. Shi, L.e. Zhang, E.M.B. Brown, A. Wu, Layered bismuth oxyhalide nanomaterials for highly efficient tumor photodynamic therapy, Nanoscale 8 (2016) 12715–12722.
[47] S.S. Lucky, N. Muhammad Idris, Z. Li, K. Huang, K.C. Soo, Y. Zhang, Titania coated upconversion nanoparticles for near-infrared light triggered photodynamic therapy, ACS Nano 9 (2015) 191–205.
[48] Y. Liu, Y. Liu, W. Bu, C. Cheng, C. Zuo, Q. Xiao, Y. Sun, D. Ni, C. Zhang, J. Liu, Hypoxia induced by upconversion-based photodynamic therapy: towards highly effective synergistic bioreductive therapy in tumors, Angew. Chem. Int. Ed. 54 (2015) 8105–8109.
[49] R. Gui, H. Jin, Z. Wang, J. Li, Black phosphorus quantum dots: synthesis, properties, functionalized modification and applications, Chem. Soc. Rev. 47 (2018) 6795–6823.
[50] Q. Yuan, Y. Wu, J. Wang, D. Lu, Z. Zhao, T. Liu, X. Zhang, W. Tan, Targeted bioimaging and photodynamic therapy nanoplatform using an aptamer-guided G-quadruplex DNA carrier and near-infrared light, Angew. Chem. Int. Ed. 52 (2013) 3965–13969.
[51] R. Xu, X. Wang, D. Wang, K. Zhou, Y. Li, Surface structure effects in nanocrystal MnO_2 and Ag/MnO_2 catalytic oxidation of CO, J. Catal. 237 (2006) 426–430.